

Lagrangian analysis of hemodynamics data from FSI simulation

Vincent Duvernois¹, Alison L. Marsden² and Shawn C. Shadden^{1,*},[†]

¹*Illinois Institute of Technology, Chicago, IL, USA*

²*University of California, San Diego, CA, USA*

SUMMARY

We present the computation of Lagrangian-based flow characterization measures for time-dependent, deformable-wall, finite-element blood flow simulations. Applicability of the algorithm is demonstrated in a fluid–structure interaction simulation of blood flow through a total cavopulmonary connection (Fontan procedure), and results are compared with a rigid-vessel simulation. Specifically, we report on several important Lagrangian-based measures including flow distributions, finite-time Lyapunov exponent fields, particle residence time, and exposure time calculations. Overall, strong similarity in Lagrangian measures of the flow between deformable and rigid-vessel models was observed. Copyright © 2012 John Wiley & Sons, Ltd.

Received 9 May 2012; Revised 13 September 2012; Accepted 21 September 2012

KEY WORDS: computational fluid dynamics; fluid–structure interaction; hemodynamics; Fontan; particle tracking; total cavopulmonary connection; transport

ABBREVIATIONS AND NOTATIONS

FEM:	finite-element mesh
FSI:	fluid–structure interaction
FTLE:	finite time Lyapunov exponent
GPU:	graphics processing unit
IVC:	inferior vena cava
LCSs:	Lagrangian coherent structures
MET:	mean exposure time
PA:	pulmonary artery
PRT:	particle residence time
SVC:	superior vena cava
TCPC:	total cavopulmonary connection
\mathbf{x} :	position vector of a fluid element or particle
\mathbf{x}_n :	position vector of node n of FEM
\mathbf{x}_n^i :	position vector of node n of FEM, which belongs to FEM element i
$\xi_p^i = (\xi_p^i, \eta_p^i, \zeta_p^i)$:	position vector of node n in natural coordinate frame of element i
\mathbf{v} :	fluid velocity vector (defined nodally)
\mathbf{u} :	fluid velocity vector relative to FEM (defined nodally)
$\mathbf{v}_m = \mathbf{v} - \mathbf{u}$:	FEM node velocity vector
\mathbf{v}_d :	mesh displacement velocity vector (defined nodally)
$\mathbf{v} = \mathbf{u} + \mathbf{v}_d$:	augmented fluid velocity vector

*Correspondence to: Shawn C. Shadden, Engineering 1, Room 243, 10 W. 32nd St., Chicago, IL, 60616, USA.

[†]E-mail: shawn.shadden@iit.edu

1. INTRODUCTION

Current state of the art in image-based blood flow modeling involves construction of a personalized computer model that serves as the computational domain for fluid dynamics simulation. The model geometry is derived from medical image data obtained from computed topography or MRI using local or global image processing techniques [1–4]. The resulting 3D model represents a truncated section of a nominally closed-loop vascular system. Therefore, proper inflow and outflow conditions must be imposed at the model inlet(s) and outlet(s) [5–8].

The natural boundaries of the fluid domain are the vessel walls. In reality, vessel walls are compliant and interact with the blood flow. In practice, vessels are often idealized as rigid for simulation purposes. Indeed, accurate modeling of *in vivo* hemodynamics has a host of challenges beyond accounting for vessel wall dynamics. And in many applications, the motions of the vessel wall induced from hemodynamic forces are negligible compared with other modeling assumptions. However, in some vessels, deformation can become relatively large; for example, around 8% circumferential cyclic strain in the thoracic aorta is typical for middle-age persons [9], and studies have demonstrated differences in wall shear stress of up to 50% at peak flow, or during exercise, in compliant aneurysms [10]. During the past several years, there has been growing progress towards modeling the interplay between vessel movement and blood flow dynamics. Several developments in FSI modeling for hemodynamics applications have been made (see, e.g., [11–15]). Efforts to increase the accuracy and efficiency of computer modeling are ongoing, as with addressing physical challenges such as the assignment of variable wall properties and external tissue support [16–18].

The aforementioned technological advances to study flow in large vessels have been directed toward improvements in modeling. The motivation behind these wide-ranging and tremendous efforts is to better understand (or possibly predict) *in vivo* blood flow conditions. From the practical standpoint, these models result in pressure and velocity data. The velocity data are used to characterize and deduce relevant flow information, for example, to diagnose clinically significant hemodynamic conditions such as recirculation, stagnation, mixing, separation, and impingement, associated with disease or remodeling. Proper postprocessing/interpretation of unsteady flow data is a significant challenge, however, and has received less attention than the derivation of the data itself. Common techniques for flow structure analysis are based on the identification of Eulerian measures to characterize coherent structures in the flow. Namely, vortex formation is the basis for turbulence and much of the complexity we observe in unsteady flow. Classic works in vortex identification include [19–21].

Eulerian characterizations have been proven effective in hemodynamics analysis under steady conditions [22]. For transport analysis, it is well documented [23, 24] that instantaneous Eulerian descriptions are often inadequate in conveying the nature of particle trajectories when the flow is unsteady. This problem is compelling for cardiovascular research, where flow through large vessels is often spatially and temporally complex, because understanding transport has far-reaching importance. Lagrangian-based methods for coherent structure identification can provide a more complete and direct characterization of unsteady hemodynamics than commonly used wall shear stress metrics [25]. Other recent metrics in Lagrangian-based hemodynamics characterization include trajectory-based helicity measures [26–28]. These works demonstrate the need for trajectory-based methods in analyzing unsteady hemodynamics.

Whereas some results exist comparing FSI versus rigid-vessel hemodynamics using instantaneous Eulerian data, for example, [11, 29, 30], to the best of our knowledge, few, if any, results exist comparing Lagrangian-based descriptions. Such comparison is compelling for at least two reasons: (1) instantaneous measures (e.g., velocity) have less direct importance to biology than the motion of the blood itself or particles transported by the blood flow and (2) small differences (e.g., modeling errors) in velocity field prediction can accumulate to large errors in predicting the actual fluid motion over time; therefore, it may be unclear how modeling assumptions, such as rigid-vessels, affect the transport topology. Our motivation is to describe the computation of Lagrangian-based criteria for flow characterization on deformable grids and to apply these methods to investigate the changes to the flow topology in deformable versus rigid-vessel hemodynamics simulations to help begin to quantify the effect of FSI to transport topology. The algorithm is described in Section 2.

In Section 3, we present the application of the methods to a TCPC model—a surgical alteration that bypasses the heart to return venous blood directly to the PAs in patients with a single-ventricle heart defect. We explore the computation of common Lagrangian-based criteria for flow characterization such as PRT, MET, and the FTLE. The results are briefly discussed in Section 4.

2. METHODS

At the foundation of Lagrangian-based postprocessing is the solution of the advection equation

$$\dot{\mathbf{x}}(t) = \mathbf{v}(\mathbf{x}, t), \quad (1)$$

for a distribution of particles. If finite-sized particles are being tracked, a dynamical model can be used to solve for the particle velocity $\mathbf{v}(\mathbf{x}, t)$ from a one-way coupling with the fluid velocity/acceleration (see, e.g., [31]). This coupling has relatively minor consequence to the methods described herein. Otherwise, particles are treated as fluid elements (tracers), and $\mathbf{v}(\mathbf{x}, t)$ represents the fluid velocity. Velocity data is almost always given discretely in space and time, and the numerical integration of Equation (1), that is,

$$\mathbf{x}(t_f) = \mathbf{x}(t_0) + \int_{t_0}^{t_f} \mathbf{v}(\mathbf{x}(\tau), \tau) d\tau, \quad (2)$$

entails the generic steps:

- A1 Specify the initial release location \mathbf{x}_p for a particle p ,
- A2 Determine the element $e(\mathbf{x}_p)$ in the FEM containing \mathbf{x}_p ,
- A3 Perform interpolation(s) of the velocity in space and time,
- A4 Evaluate the integral in Equation (2) over a small time step Δt using appropriate quadrature,
- A5 Update particle position Δt in time and repeat from step A2 until t_f is reached.

The main challenges with particle tracking on deformable unstructured grids are (A2) tracking which element the particle is located in and (A3) interpolating the velocity so that particle advection is consistent with the mesh deformation. Herein, it is assumed that mesh topology (connectivity) remains fixed and the nodal coordinates of the mesh, and velocity defined at each node, change over time. Modification to the algorithm for simulations where the FEM topology changes over time is discussed in Section 4. We assume tetrahedral elements because they are frequently used in finite-element formulations of image-based CFD; we comment on the use of other element types in Section 4.

2.1. Element search

As a particle is integrated, the element containing the particle must be tracked. During the integration, we can locate the bounding element using a *local search* starting from the element that contained the particle at the previous time step. This strategy is highly efficient. When first initializing the integration, an appropriate seed or guess element to start this local search may not be obvious. There are alternative strategies to initially locate the element containing the particle (A1 \rightarrow A2). Common methods are often based on the use of a structured auxiliary mesh approach, which may leverage an efficient tree-based storage/search paradigm.

Let \mathbf{v} be the material (absolute) fluid velocity and \mathbf{v}_m be the velocity of the mesh nodes. Both fields are defined at nodal locations \mathbf{x}_n for $n = 1, \dots, N_{\text{nodes}}$, and times t^q for $q = 1, \dots, N_{\text{outputs}}$. Let \mathbf{x}_n^i denote the nodal coordinates of element i . The subscripts for a particular element i define the connectivity. Define the relative fluid velocity \mathbf{u} by $\mathbf{u} = \mathbf{v} - \mathbf{v}_m$ at all points (\mathbf{x}_n^i, t^q) in space–time. To integrate a particle p , the velocity of the particle at its current position and time, $\mathbf{x}_p(t_p)$, is needed. For some quadrature methods, the velocity is required at multiple nearby points in space–time to approximate the change in velocity over the time step. Because this detail requires only slight algorithmic modification, a single arbitrary point in space–time is considered here. This could be adapted to maintain consistency in problems with higher order basis functions.

The positions of the nodal coordinates, and hence geometries of the elements, are in general not defined at time t_p . To locate the element containing $\mathbf{x}_p(t_p)$, the nodal coordinates of the elements at time t_p must be computed. These can be obtained by

$$\mathbf{x}_n^i(t_p) = \mathbf{x}_n^i(t^q) + \int_{t^q}^{t_p} \mathbf{v}_m \, dt, \tag{3}$$

where $t_p \in (t^q, t^{q+1})$. The solution to Equation (3) is susceptible to modeling and truncation errors. Consequentially, it is unlikely that solving Equation (3) for $t_p = t^{q+1}$ would give the known value for $\mathbf{x}_n^i(t^{q+1})$. To ensure consistency with the mesh movement, we instead linearly interpolate the node positions in time as

$$\mathbf{x}_n^i(t_p) = \mathbf{x}_n^i(t^q) \left[1 - \frac{t_p - t^q}{t^{q+1} - t^q} \right] + \mathbf{x}_n^i(t^{q+1}) \frac{t_p - t^q}{t^{q+1} - t^q}, \tag{4}$$

where $t_p \in [t^q, t^{q+1}]$. This disregards the mesh velocity; however, this field is used in the interpolation step described in the succeeding sections. In practice, only the nodes for the guess element for the particle being considered are interpolated in time. Note that Equation (4) is consistent with the linear interpolation used to interpolate the velocity data, whereby it is assumed linear basis functions were used in the finite-element formulation.

2.2. Coordinate transformation

To determine if $\mathbf{x}_p(t_p)$ is in element i at time t_p , the natural coordinates of the element can be used. Let $\xi_p^i = (\xi_p^i, \eta_p^i, \zeta_p^i)$ denote the coordinates obtained by mapping \mathbf{x}_p from physical space to the natural coordinates of element i . The inverse transformation $\xi_p^i \mapsto \mathbf{x}_p$ is straightforward and given by

$$\mathbf{x}_p = \mathbf{x}_1^i + (\mathbf{x}_2^i - \mathbf{x}_1^i) \xi_p^i + (\mathbf{x}_3^i - \mathbf{x}_1^i) \eta_p^i + (\mathbf{x}_4^i - \mathbf{x}_1^i) \zeta_p^i. \tag{5}$$

Through a slight abuse of notation, we have used a local numbering subscript so that $k = 1, 2, 3, 4$ for \mathbf{x}_k^i , denoting the coordinates of the four nodes of tetrahedron i . Recall that $\mathbf{x}_k^i(t_p)$ are first obtained through interpolation in time by Equation (4). Equation (5) can be inverted to give

$$\xi_p^i = \frac{1}{|A|} A \mathbf{x}_p, \tag{6}$$

where $|A|$ denotes the matrix determinant, and the entries of matrix A are

$$\begin{aligned} a_{11} &= (z_4 - z_1)(y_3 - y_4) - (z_3 - z_4)(y_4 - y_1) \\ a_{21} &= (z_4 - z_1)(y_1 - y_2) - (z_1 - z_2)(y_4 - y_1) \\ a_{31} &= (z_2 - z_3)(y_1 - y_2) - (z_1 - z_2)(y_2 - y_3) \\ a_{12} &= (x_4 - x_1)(z_3 - z_4) - (x_3 - x_4)(z_4 - z_1) \\ a_{22} &= (x_4 - x_1)(z_1 - z_2) - (x_1 - x_2)(z_4 - z_1) \\ a_{32} &= (x_2 - x_3)(z_1 - z_2) - (x_1 - x_2)(z_2 - z_3) \\ a_{13} &= (y_4 - y_1)(x_3 - x_4) - (y_3 - y_4)(x_4 - x_1) \\ a_{23} &= (y_4 - y_1)(x_1 - x_2) - (y_1 - y_2)(x_4 - x_1) \\ a_{33} &= (y_2 - y_3)(x_1 - x_2) - (y_1 - y_2)(x_2 - x_3), \end{aligned} \tag{7}$$

where (x_k, y_k, z_k) are the components of \mathbf{x}_k^i .

The advantage of natural coordinates is that they simplify element searching (and interpolation as discussed in the next section). Point \mathbf{x}_p is in element i if

$$\xi_p^i \geq 0, \quad \eta_p^i \geq 0, \quad \zeta_p^i \geq 0, \quad \text{and} \quad 1 - \xi_p^i - \eta_p^i - \zeta_p^i \geq 0. \tag{8}$$

If the point is not in the element, a local search strategy can be used to find the element containing the point by considering the most violated condition, which indicates the neighboring element that should be used as the next guess [32] (cf. Algorithms 1 and 2). This last step requires element

adjacency information, which is typically available during mesh generation or can be computed as a preprocessing step. Note that element adjacency should be ordered so the most violated condition can be matched to the correct neighbor to use as the next guess for evaluating Equations (6) and (8). Because boundary elements have faces that are not shared with another element, if the local search proceeds in the direction of a boundary face, the search returns a failure, indicating the point has been advected outside of the domain. This element search method converges quickly but can fail if there is no convex hull containing guess element i and element $e(x_p)$. This almost never occurs if the CFL condition is close to, or less than, 1, which is required nonetheless for accurate integration of Equation (1) from the FEM data.

2.3. Velocity interpolation

An additional step is imposed to ensure that particle integration is consistent with the mesh deformation. The mesh is updated by the FSI solver, and nodal coordinates and velocities are output at (usually arbitrarily chosen) discrete times t^q . For postprocessing, particle trajectories are solved by integration of the output field data. However, the output resolution, subsequent interpolation, or particle time-stepping scheme may not be consistent with the FSI time-stepping of the FEM mesh. This can be a problem for particles close to the wall, as it can result in significant ‘leakage’ of particles and hence significant errors in nearly all Lagrangian criteria used to quantify the flow topology.

To resolve this issue, a displacement velocity \mathbf{v}_d is defined at each point (\mathbf{x}_n^i, t^q) by the finite difference

$$\mathbf{v}_d(\mathbf{x}_n^i, t^q) = \frac{\mathbf{x}_n^i(t^{q+1}) - \mathbf{x}_n^i(t^q)}{t^{q+1} - t^q}, \quad (9)$$

and an augmented velocity is defined as

$$\begin{aligned} \mathbf{v}(\mathbf{x}_n^i, t_q) &= \mathbf{v}(\mathbf{x}_n^i, t_q) - \mathbf{v}_m(\mathbf{x}_n^i, t_q) + \mathbf{v}_d(\mathbf{x}_n^i, t_q) \\ &= \mathbf{u}(\mathbf{x}_n^i, t_q) + \mathbf{v}_d(\mathbf{x}_n^i, t_q) \end{aligned} \quad (10)$$

In this way, the integration of a particle is consistent with the deformation of the FEM as represented by the data. This approach decouples the algorithm from the underlying FSI scheme.

Once the element i containing the particle at time t_p is determined using the aforementioned methods, temporal interpolation over the interval (t^q, t^{q+1}) is used to evaluate the velocity at the nodes of element i at time t_p , for example, linear interpolation yields

$$\mathbf{v}_k^i(t_p) = (1 - \delta_{t_p}) \mathbf{v}_k^i(t^q) + \delta_{t_p} \mathbf{v}_k^i(t^{q+1}), \quad (11)$$

where $\delta_{t_p} = [t_p - t^q]/[t^{q+1} - t^q]$, and $k = 1, 2, 3, 4$.

The velocity is then interpolated in space at the particle location. Volume-weighted or linear basis function interpolation methods are mathematically equivalent. Because the natural coordinates $(\xi_p^i, \eta_p^i, \gamma_p^i)$ have already been computed during the element search step, linear basis functions are an efficient choice because of their simple form in natural coordinates. Specifically,

$$\begin{aligned} \mathbf{v}(\mathbf{x}_p, t_p) &= \mathbf{v}(\xi_p^i, t_p) \\ &= \mathbf{v}_1^i(t_p) + [\mathbf{v}_2^i(t_p) - \mathbf{v}_1^i(t_p)] \xi_p^i(t_p) + [\mathbf{v}_3^i(t_p) - \mathbf{v}_1^i(t_p)] \eta_p^i(t_p) \\ &\quad + [\mathbf{v}_4^i(t_p) - \mathbf{v}_1^i(t_p)] \zeta_p^i(t_p). \end{aligned} \quad (12)$$

Runge–Kutta schemes that require velocity information at intermediate times must interpolate the velocity at locations in the neighborhood of the particle’s position in space–time for each update step. These intermediate interpolations may lie in different tetrahedra. Therefore, element search(s) may be needed during the update step; however, this can be performed efficiently using the same local search method that was used to track the particle in the velocity mesh between update steps. The mesh size and temporal resolution in most applications are such that mesh and velocity data are too large for the entire time history to be loaded into memory at once; therefore, a shifting data window is required during implementation.

2.4. Boundary treatment

Because of interpolation, some percentage of particles will cross no-slip boundaries even if time step sizes are set to satisfy the CFL restriction, and the advection scheme is consistent with the mesh displacement. For example, this can occur for rigid-vessel simulations with $CFL \ll 1$. Inflow and outflow faces can be tagged, and when the local element search fails for a particle, one can difference the position data before and after the integration step to determine if it crossed (legitimately) an inlet/outlet or (illegitimately) a vessel wall. When boundary crossing occurs, the integration procedure or interpolation can be modified; for example, the step size can be adapted. The computational overhead for determining if a particle crossed a no-slip boundary becomes unwieldily in most realistic applications, and, nonetheless, adaptive step sizing or changes to ‘boundary layer’ interpolation functions have been proven not to be efficient or robust in our experience. It is more efficient to replace no-slip boundaries with small inward flux boundaries that effectively negate or reverse a particle’s outward normal velocity component (as may be expected for when a cell or other particle collides with the vessel wall). This is performed by extracting the no-slip boundaries and computing the inward normals at each node as a preprocessing step. When velocity frames are loaded into memory during particle integration, a slight inward component is added to v_m on boundary nodes. This modification has minimal overhead, only affects particles inside boundary elements, and varies smoothly to zero over the boundary element. In practice, the value can typically be set such that the local CFL condition for the flux velocity is at least three orders of magnitude less than 1; that is, a very small but finite ‘inflow’ is needed to prevent leakage due to truncation errors. In such cases, the advection errors introduced have been shown to be indistinguishable/negligible when compared with more rigorous but inefficient adaptive time-stepping [33].

2.5. Initial mapping

The particle initialization ($A1 \rightarrow A2$) for a deformable mesh requires extra attention than for a fixed mesh. For analysis of time-dependent flows, it is common to seed multiple particle grids. For example, in the computation of FTLE, PRT, or other Lagrangian-based fields, grids of particles are released over time. For data on a fixed mesh, the initialization of the particle grid only needs to be performed once, and element location data can be reused for subsequent releases. This is important because initial cell location can be more costly than subsequent local searching methods. With deformable mesh data, one needs to adapt the release locations. Because locations in physical space change relative to the model, particles, for example, seeded over a model inlet, at one instance cannot be released at the same locations later because the location relative to the model may have changed. Initial particle locations are typically specified in physical coordinates or at least relative to the vascular model at a fixed instance in time. Therefore, when computing Lagrangian field data, each particle in the first release is located by its bounding element and corresponding natural coordinates. This information is stored, and subsequent particles are released from the same locations in natural (not physical) coordinates.

3. RESULTS

Here, we apply the particle tracking algorithm to a model of a TCPC, also known as the Fontan procedure, a surgery performed in the palliation of single ventricle heart defects [34, 35]. This surgery has been studied extensively by computer modeling [36–41], including FSI simulations [29, 30, 42], which makes it a compelling application to compare advective transport characteristics between FSI and rigid-vessel simulations.

3.1. Model construction

A 3-year-old male patient post-Fontan surgery underwent routine clinical contrast-enhanced MRI using a 1.5T scanner. The use of this data had institutional review board (IRB) approval. Anatomic images were acquired using 3D fast gradient-recalled echo sequences during breath-hold. Resulting bright blood image stacks were used to construct an anatomically accurate computer model of the

TCPC using a custom version of the software package ‘SimVascular’ [43]. Additional imaging parameters were described in [40].

3.2. Boundary conditions

Volumetric flow data was measured by phase-contrast (PC) MRI at the IVC and SVC using cardiac gating with respiratory compensation. The SVC volumetric flow data were mapped to the model’s SVC inlet using a time-dependent uniform profile. Because respiration strongly affects the IVC flow waveform [44], an IVC flow rate model was derived from assimilation of PC MRI velocity data and pressure tracings from catheterization. This was an iterative process whereby full simulations were used to tune the inflow waveform so that *in vivo* pressure tracings were replicated [45]. Three-element Windkessel (RCR) models were coupled to the outlet faces of the PAs. The resistances and capacitances were also adjusted in the tuning iterations on the basis of pressure tracing and morphological data using methods described in [40,46]. The vessel walls of the PAs, SVC, and the IVC Gore-Tex conduit were assigned variable wall properties. The elastic coefficient of the conduit was based on manufacturer data. Elasticity for the PAs was derived from [47], and the IVC was assumed 10% more elastic than the PAs on the basis of the observation from the PC MRI data. Wall thickness was assigned at the inlets and outlets on the basis of vessel diameter and solved for in the interior using the Laplace equation method proposed in [42].

3.3. Flow solver

Blood was modeled as an incompressible, Newtonian fluid by the Navier–Stokes equations. For the FSI simulation, an ALE formulation of the incompressible Navier–Stokes equations was solved using a residual-based variational multiscale FEM [48]. Details of the formulation and solution procedure were contained in [42]. The same solver was used for the rigid-vessel simulation. This solver uses a second-order generalized- α integration scheme. Adaptive meshing was used for improved accuracy. The mesh for both rigid and deformable simulations is displayed at maximum flow in Figure 1.

3.4. Hepatic flow distribution

Hepatic flow distribution is important for lung development in TCPC patients because of a hepatic factor present in the IVC blood [49,50]. Clinical studies have shown that IVC flow should be well distributed to prevent the formation of pulmonary arteriovenous malformations and that correction of uneven distribution can lead to regression of pulmonary arteriovenous malformations. Because SVC and IVC flow mix at the junction, distribution of IVC blood not only cannot be determined by relative flow rate data but also depends on the junction geometry and unsteady flow dynamics.

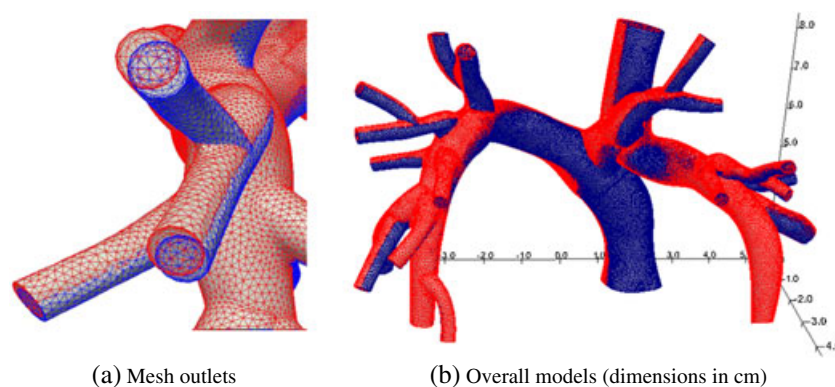


Figure 1. Fluid–structure interaction mesh (red) superimposed on rigid mesh (blue) at peak flow. The grids are initially aligned.

Table I. SVC and IVC flow distribution data.

Model	Release	LPA	RPA
Rigid	IVC	88.45%	11.59%
	SVC	13.74%	86.23%
	Total	44.73%	55.30%
FSI	IVC	89.21%	10.80%
	SVC	15.87%	84.13%
	Total	44.49%	55.52%
Difference	IVC	0.76%	0.76%
	SVC	2.14%	2.14%
	Total	0.24%	0.24%

SVC, superior vena cava; IVC, inferior vena cava; FSI, fluid–structure interaction; LPA, left pulmonary artery; RPA, right pulmonary artery.

To compute flow splits for both inflow tracks, we simulated a uniform density of particles released at each inlet (IVC and SVC). Specifically, particles were released across both inlets such that particle influx was proportional to the local flow rate at each release location over time. This ensured that a spatially uniform density of particles was released into the model over time. Because the inflow was periodic, particles were only released over one cycle but were integrated over 10 cycles to ensure that all particles were flushed from the domain so their final destination (RPAs or LPAs) could be properly assessed. Results for rigid and FSI simulations are summarized in Table I. For both rigid and FSI simulations, to ensure the convergence of the results, we used two seeding densities. Distribution data were computed from seeding particles using a spacing of 500 microns and a spacing of 200 microns (more than 15-fold the original particle density). The latter resulted in several million particles released over one cycle. The maximum change in the results between the two seeding densities was 0.077%.

3.5. Finite time Lyapunov exponent/Lagrangian coherent structure computation

The computation of LCS has gained traction over the past several years for studying transport in wide-ranging fluid applications (see [51] for a review). LCSs were first applied to study blood flow in [25] and have subsequently been applied in several cardiovascular applications [33, 52–54]. LCSs are typically computed from FTLE fields. The FTLE measures the sensitivity of particle trajectories to changes in their initial position. Specifically, the flow map, $\phi_{t_0}^{t_f} : \mathbf{x}(t_0) \mapsto \mathbf{x}(t)$, is obtained from Equation (2) using the algorithm described in Section 2. The FTLE, Λ , is defined as

$$\Lambda(x_0, t_0; t_f) = \frac{1}{|t_f - t_0|} \ln \left\| \nabla \phi_{t_0}^{t_f}(\mathbf{x}_0) \right\|, \quad (13)$$

where $\mathbf{x}_0 = \mathbf{x}(t_0)$. The FTLE field is sampled over the fluid domain by seeding a grid of particles $\{\mathbf{x}_0\}$ that are advected from t_0 to t_f by the flow $\phi_{t_0}^{t_f} : \{\mathbf{x}(t_0)\} \mapsto \{\mathbf{x}(t)\}$. This enables Equation (13) to be evaluated at each initial locations \mathbf{x}_0 . This is repeated over a sequence of times t_0 to compute the evolution of the field over time (cf. [25]). For the TCPC model, dense grids of particles were seeded over the IVC and SVC sequentially over one period of the flow. For each seed time, the released particles were integrated for 10 cycles or until they had been flushed from the domain. The final locations of these particles were used to evaluate Equation (13).[‡]

Lagrangian coherent structures are revealed in the FTLE field as hypersurfaces that locally maximize the FTLE measure [55, 56]. These structures are distinguished material surfaces (or ‘transport barriers’) that can often be identified as boundaries to regions with dynamically distinct behavior

[‡]The FTLE for each point was computed when the particle, or a neighbor, left the domain as described in [25, 55].

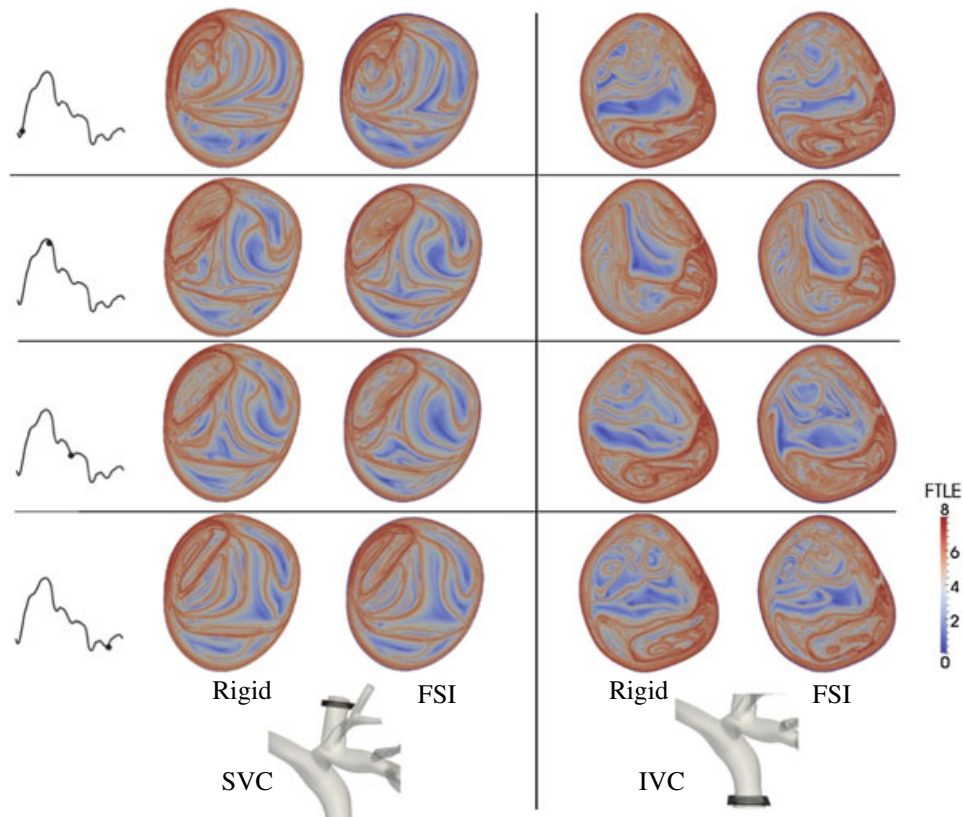


Figure 2. Comparison of the finite time Lyapunov exponent fields and corresponding Lagrangian coherent structures taken at cross sections to the inferior vena cava (IVC) and superior vena cava (SVC) at the specified points of the cycle (referenced to the IVC inflow waveform). FSI, fluid–structure interaction.

(e.g., boundaries to vortices [57, 58], flow separation, or attachment profiles [55, 59], kinematic mixing [60], etc.). Figure 2 shows cross sections of the FTLE fields in the IVC and SVC at various time points for the FSI and rigid-vessel simulation. The curves of high FTLE correspond to cross sections of 2D LCS surfaces embedded in the flow. Several of the LCSs represent boundaries between regions that are mapped to different PAs, most prominently between the LPA and RPA tracks.

3.6. Particle residence time

A common method to quantify recirculation and stagnation in cardiovascular flows is the PRT [61, 62]. This measure is thought to be clinically important because a region with poor particle clearance due to high recirculation and stagnation may lead to platelet aggregation, mural thrombus, and wall inflammation (early atheroma). Mathematically, PRT can be represented by the equation

$$\text{PRT}(\mathbf{x}_0, t_0; D) = \min(\tau) \in (0, \infty) : \mathbf{x}(\mathbf{x}_0, t_0 + \tau) \notin D. \quad (14)$$

The PRT at position \mathbf{x}_0 at time t_0 is the minimum time needed for a particle trajectory $\mathbf{x}(t)$ starting at \mathbf{x}_0 at time t_0 to leave the subset D of the fluid domain. To compute PRT for the TCPC, a dense grid of particles was seeded in the IVC and SVC at several times. The particles were integrated for 10 cycles or until they were flushed from the domain. Equation 14 was evaluated by choosing D as the entire TCPC model. Results of the PRT calculations are shown in Figure 3 over the same cross sections in the SVC and IVC, and same times in the cycle, as for the FTLE results in Figure 2. As shown, the majority of the particles are flushed from the model in less than 1 s.

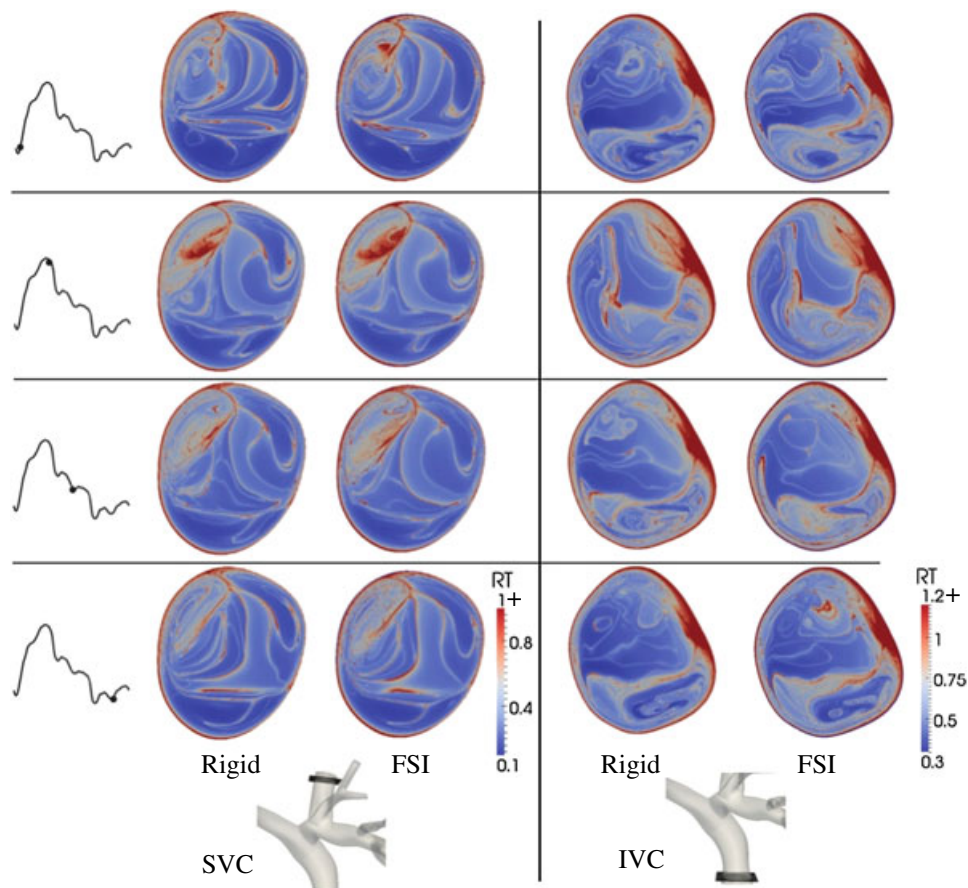


Figure 3. Comparison of the particle residence time fields taken at cross sections to the inferior vena cava (IVC) and superior vena cava (SVC) at the specified points of the cycle (referenced to the IVC inflow waveform). FSI, fluid–structure interaction.

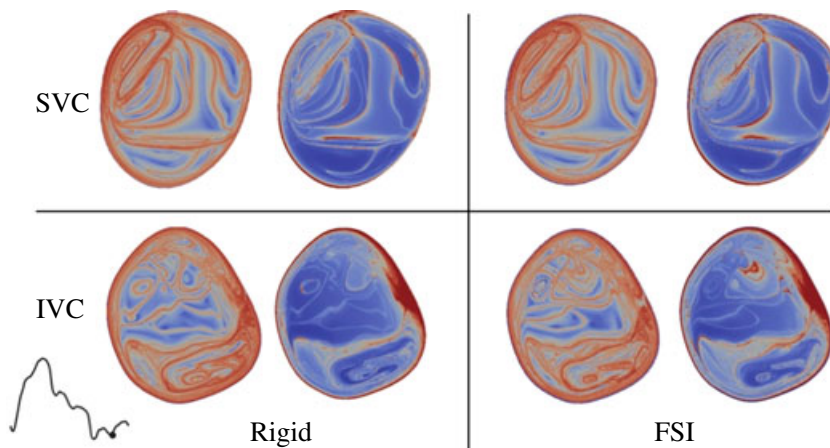


Figure 4. Comparison of the finite time Lyapunov exponent (left in each quadrant) and particle residence time (right in each quadrant) fields at the inferior vena cava (IVC) and superior vena cava (SVC) levels during diastole. The fields compare similarly at other points in time. FSI, fluid–structure interaction.

A comparison of the FTLE and PRT fields in Figure 4 shows a strong correlation between locations of LCS and high PRT, and boundaries between various regions with distinct PRT values. Specifically, several LCSs shown represent boundaries between flow to different PAs. As such,

these LCSs represent attachment profiles, attaching to stagnation lines at vessel bifurcations. Therefore, particles along (or near to) these surface stagnate into the vessel wall, resulting in elevated PRT. In addition, other LCS may represent boundaries to regions of recirculation, and hence bound regions with elevated PRT values, as described in [25].

3.7. Mean exposure time

The PRT measure does not give information on where particles travel through the domain or how long they reside in particular subsets of D . For example, it may not be clear whether locally high PRT indicates a region of stagnation, a region of recirculation, or a region where particles become entrained into subsequent low or recirculating flow. In addition, particles farther upstream will, on average, have higher PRT than those downstream because upstream particles naturally take longer to flush from any given domain. To address these issues, alternative measures of ‘residence time’ have been proposed. In [63], a measure, similar to the one in [64], was proposed to quantify the MET of regions of the vascular domain to better localize flow stasis information. To compute MET, the fluid domain is discretized into MET elements; for example, the FEM defining the velocity data can be used or an independent auxiliary mesh. Particles are advected through the domain and tracked. For each MET element, the number of particles passing through the element and how long each particle resides in the element are computed. The MET for element e was defined as

$$\text{MET}(e) = \frac{1}{N_e \sqrt[3]{V_e}} \sum_{p=1}^{N_p} \int_0^{\infty} \chi_e(p, t) dt, \quad (15)$$

where N_e is the number of ‘encounters’ of a particle passing through the element e , V_e is the volume of element e , and N_p is the total number of particles released,

$$\chi_e(p, t) = \begin{cases} 1 & \text{if } \mathbf{x}_p(t) \in e, \\ 0 & \text{if } \mathbf{x}_p(t) \notin e, \end{cases} \quad (16)$$

and $\mathbf{x}_p(t)$ is the position of particle p at time t . Note that a recirculating particle that revisits the same MET element contributes less than a stagnant particle that spends an equivalent time in the element because of the N_e normalization. The proposed measure captures both stagnation and recirculation, with recirculation being a lower ‘risk’ than stagnation, as may be expected clinically. The measure is inversely proportional to the length scale of the MET element, as measured by $\sqrt[3]{V_e}$, because the transit time of an element is proportional to the element length, not volume, for elements that are sufficiently small. For grids with elements highly skewed in the direction of flow, a more appropriate length scale should be used.

To compute MET in the TCPC models, the domain was seeded with particles with uniform spacing of 150 microns. Particles were released from the inlets of the SVC and IVC on the basis of the flow rate at each release location over time to ensure a uniform inflow. This resulted in slightly over

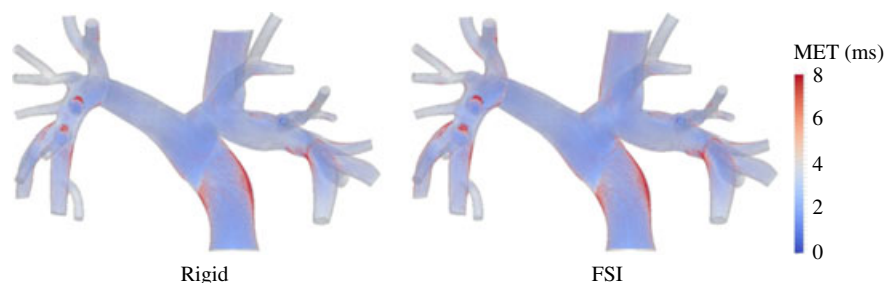


Figure 5. Comparison of the mean exposure time (MET) fields for rigid-vessel and fluid–structure interaction (FSI) simulations.

5.5 million particles released over one cycle.[§] The particles were tracked for 10 cycles or until they were flushed from the domain. Elements in the velocity mesh were used as MET elements. The results of the MET computations for the FSI and rigid-vessel simulations are shown in Figure 5.

4. DISCUSSION

Overall, we observed strong similarity in Lagrangian measures of the flow between FSI and rigid-vessel TCPC models. Because the flow is chaotic, a pointwise comparison between the fields is not well posed. A statistical comparison could be performed (e.g., Bland–Altman analysis); however, the FTLE fields enabled us to reveal LCS, which are intrinsic structures in the flow that control mechanisms of transport. Therefore, comparison of these structures enables us to assess if there are any topological differences in the flow directly. The same LCSs were observed in the FSI and rigid-vessel simulations, at least for the most well-defined structures (i.e., those with high and sharp FTLE values). The shape of a particular LCS varied slightly in some cases, but few additional (dominant) features were completely absent in one simulation or the other. Only small scale LCS in regions of high mixing varied. Because of the high sensitivity of trajectories to initial conditions (as measured by the FTLE) in these regions, the flow topology in these regions also varied, for example, from cycle to cycle. Therefore, it is difficult to attribute the differences of FTLE/LCS in such regions to vessel deformation alone. Nonetheless, because the primary LCSs were persistent between FSI and rigid-vessel simulations, the main topological features controlling transport appeared to not be significantly influenced by the vessel deformation. The similarity of the fields also gives verification that the particle tracking algorithm is properly implemented. In more highly complex flows, or flows with large vessel deformations, this may be more difficult to assess because in such cases, differences resulting from implementation errors could potentially be masked by differences in the flow physics themselves.

It is of general importance to have the capability to quantify advective processes from FSI simulation results for two main reasons. First, FSI simulations generally provide a more complete physical modeling of blood flow conditions, and in some cases are necessary to accurately model *in vivo* conditions. Therefore, the general importance of FSI modeling of hemodynamics simulation motivates the need to develop tools to analyze FSI data. Second, Lagrangian measures provide more direct evaluation of unsteady hemodynamics data, and in particular evaluation of inherently advective-driven processes that are thought to be important to vascular health. For example, [25] demonstrated that LCS can be used to evaluate mechanisms for flow stagnation and recirculation; vortex formation, entrainment, detrainment, and interaction; and flow separation, attachment, and impingement in cardiovascular flow. All of these phenomena are potentially important to vascular health.

Additionally, comparison of the flow topologies directly from flow solver data, for example, velocity data or instantaneous fields derived from it, is potentially problematic because small differences in the velocity field resulting from rigid versus deformable vessel modeling may lead to large differences in particle trajectories because velocity field errors become integrated. For the application herein, a rather surprising result was that although vessel displacements around 10% were observed, this appeared to have little effect to the flow topology. It should be noted, however, that mesh displacement often results from translational motions that may have less influence to flow topology than localized strains. For the application herein, it is likely that the flow topology is dominated by vessel morphology and inflow and outflow conditions. This is consistent with previous observations of the primary importance of patient-specific modeling and physiologic boundary conditions to hemodynamics simulation [65]. This does not imply that vessel deformation has negligible influence to vascular flow topology in general.

The FTLE or PRT could have been plotted anywhere in the model for comparison. Choosing cross sections near the SVC and IVC inlet planes enabled us to display results on the basis of the advection of the particles through the ‘entire’ model. That is, because the divergence of a particle’s trajectory between two flow fields will in general increase the longer the particle is advected, plotting FTLE

[§]Because there are over 1 million MET elements and several million particles, an efficient implementation of Equation (15) is required (see [63]).

and PRT results near the inlet planes provided a more ‘complete’ comparison than choosing cross sections elsewhere in the model because PRT and FTLE values for a trajectory are plotted at the trajectory’s initial location. This point is less relevant to the MET field, which by construction is derived everywhere from particle advection through the model. The flow distribution data presented in Table I were consistent with the flow distribution data presented by [18], which were based on the solution of an advection–diffusion equation over the FEM than on particle tracking as used herein.

With regard to performance, particle tracking on deformable grids requires additional processing and memory requirements than particle tracking on a fixed mesh. For large numbers of particles typically used for Lagrangian field computations, the increase in processing primarily comes from the interpolation in time of the node coordinates of the FEM elements (lines 1–7 in Algorithm 2). In general, we noticed about a 20% increase in processing time, but this varied depending on the platform and computation. Additional processing for particle initialization and computing the augmented velocity \mathbf{v} have less influence on the overall computation time. Particles are typically non-interacting, and integration can be readily parallelized; GPUs and accelerated processing units have become favored architectures for this task [66]. In such cases, memory overhead becomes the bottleneck. For fixed mesh computations, only the velocity data needs to be streamed. It has been our experience that this already complicates GPU-based computation for rigid-vessel particle tracking on large-scale meshes. For FSI computation, the nodal coordinates (and surface normals if boundary treatment in Section 2.4 is used) also need to be streamed. Our experience has been that these additional requirements, in addition to additional registry usage with an increased number of variables, greatly diminish GPU utilization and speedup.

The use of tetrahedral elements is common in finite-element analysis, and the algorithm used herein leverages this topology. Other element types may be used, particularly with other FSI formulations. The main change for other element types is the cell search procedure, assuming isoparametric elements. Particularly the mapping from physical to natural coordinates of the test element, that is, the analog to Equation (6), must be computed. More importantly, for other element types, there is generally not a convenient manner by which to determine a local search protocol as

Algorithm 1 Returns element index containing coordinates y at time t . Start search from element index e .

```

function LOCALELEMENTSEARCH( $e,t,y$ )
  while 1 do
     $z = \text{GETNATURALCOORDINATES}(e,t,y);$  ▷ See Alg. 2
     $d = \min(z[1], \min(z[2], \min(z[3], 1 - z[1] - z[2] - z[3])))$ ;
    if  $d \geq 0$  then ▷  $y$  inside element  $e$  at time  $t$ 
      return  $e$ ;
    else ▷ Reset guess element
      if  $z[1] - d \equiv 0$  then
         $e = \text{Elements}[e].\text{NeighborIndex}[0];$ 
      else if  $z[2] - d \equiv 0$  then
         $e = \text{Element}[e].\text{NeighborIndex}[1];$ 
      else if  $z[3] - d \equiv 0$  then
         $e = \text{Elementy}[e].\text{NeighborIndex}[2];$ 
      else
         $e = \text{Element}[e].\text{NeighborIndex}[3];$ 
      end if
      if  $e == -1$  then ▷ Search proceeded outside domain
        return  $e$ ;
      end if
    end if
  end while
end function

```

Algorithm 2 Maps physical coordinates y into the natural coordinates z of element e at time t . Assumes velocity and nodal coordinates at two times are streamed into memory.

```

function GETNATURALCOORDINATES(e, t, y)
  tloc = (t - Velocity[0].Time) / (Velocity[1].Time - Velocity[0].Time);
  for i=1  $\rightarrow$  4 do                                      $\triangleright$  Loop over element's nodes
    for j = 1  $\rightarrow$  3 do                                    $\triangleright$  Loop over node coordinates
      x[i][j] = (1-tloc) * Nodes[0][Elements[e].NodeIndex[i]].X[j] + ...
      tloc * Nodes[1][Elements[e].NodeIndex[i]].X[j];      $\triangleright$  Equation (4)
    end for
  end for
  a = COMPUTEMATRIX(x);                                 $\triangleright$  Returns matrix  $a_{ij}$  defined by Equation (7)
  v = COMPUTEDETERMINANT(a);                            $\triangleright$  Returns determinant  $v$  of matrix  $a$ 
  for j = 1  $\rightarrow$  3 do
    z[i] = (a[i][1] * (y[1] - x[1][1]) + a[i][2] * (y[2] - x[1][2]) + a[i][3] * (y[3] - x[1][3])) / v;
     $\triangleright$  Equation (5)
  end for
  return z;
end function

```

described in Algorithms 1 and 2. In fact, this local search protocol performs comparable with interpolation on Cartesian grids where element searching becomes trivial. For this reason, we have found it more efficient to tetrahedralize other grid types as a preprocessing step so the algorithm herein can be applied.

Here, we considered particle tracking on meshes with fixed topology. For FSI problems that involve large displacements, such as in problems with nonlinear membrane motion, buckling, or volume contraction, remeshing may be required to prevent significant skewing of the elements. For such data sets, it is difficult to interpolate velocity data between time points when the topological changes occur. That is, the element bounding any particular particle is not well defined during such time intervals because the element nodes cannot in general be interpolated in time. This problem can be addressed. Consider the velocity mesh at the latter time denoted by $\{y(t_{i+1})\}$ and the previous mesh as $\{x(t_i)\}$. The velocity field at the nodes of grid $\{y\}$ can be interpolated at time t_i using the velocity field defined on $\{x(t_i)\}$. If the two meshes share a majority of nodes (which is typical in remeshing), then this step can be restricted to the new nodes/elements, but this requires consistent node ordering and connectivity between remeshing.

ACKNOWLEDGEMENTS

We would like to sincerely thank Yuri Bazilevs (UCSD) and Christopher Long (USCD) for FEM simulation results used in this study, and Jeffrey Feinstein (Stanford) and Frandics Chan (Stanford) for the corresponding patient image data. This work was supported in part by the Burroughs Wellcome Fund CASI program (ALM).

REFERENCES

1. Wang K, Dutton R, Taylor C. Improving geometric model construction for blood flow modeling. *IEEE Engineering in Medicine and Biology Magazine* 1999; **18**(6):33–39. DOI: 10.1109/51.805142.
2. Antiga L, Ene-Iordache B, Remuzzi A. Computational geometry for patient-specific reconstruction and meshing of blood vessels from MR and CT angiography. *IEEE Transactions on Medical Imaging* 2003; **22**(5):674–684. DOI: 10.1109/TMI.2003.812261.
3. Yim P, Vasbinder G, Ho V, Choyke P. Isosurfaces as deformable models for magnetic resonance angiography. *IEEE Transactions on Medical Imaging* 2003; **22**(7):875–881. DOI: 10.1109/TMI.2003.815056.
4. Cebal J, Castro M, Appanaboyina S, Putman C, Millan D, Frangi A. Efficient pipeline for image-based patient-specific analysis of cerebral aneurysm hemodynamics: technique and sensitivity. *IEEE Transactions on Medical Imaging* 2005; **24**(4):457–467. DOI: 10.1109/TMI.2005.844159.

5. Formaggia L, Gerbeau J, Nobile F, Quarteroni A. On the coupling of 3D and 1D Navier–Stokes equations for flow problems in compliant vessels. *Computer Methods in Applied Mechanics and Engineering* 2001; **191**(6-7):561–582. DOI: 10.1016/S0045-7825(01)00302-4.
6. Vignon-Clementel IE, Figueroa CA, Jansen KE, Taylor CA. Outflow boundary conditions for three-dimensional finite element modeling of blood flow and pressure in arteries. *Computer Methods in Applied Mechanics and Engineering* 2006; **195**(29-32):3776–3796. DOI: 10.1016/j.cma.2005.04.014.
7. Migliavacca F, Balossino R, Pennati G, Dubini G, Hsia T, de Leval M, Bove E. Multiscale modelling in biofluid dynamics: application to reconstructive paediatric cardiac surgery. *Journal of Biomechanics* 2006; **39**(6):1010–1020. DOI: 10.1016/j.jbiomech.2005.02.021.
8. Kim HJ, Vignon-Clementel IE, Figueroa CA, LaDisa JF, Jansen KE, Feinstein JA, Taylor CA. On coupling a lumped parameter heart model and a three-dimensional finite element aorta model. *Annals Of Biomedical Engineering* 2009; **37**(11):2153–2169. DOI: 10.1007/s10439-009-9760-8.
9. Morrison TM, Choi G, Zarins CK, Taylor CA. Circumferential and longitudinal cyclic strain of the human thoracic aorta: age-related changes. *Journal of Vascular Surgery* 2009; **49**(4):1029–1036. DOI: 10.1016/j.jvs.2008.11.056.
10. Bazilevs Y, Hsu MC, Zhang Y, Wang W, Liang X, Kvamsdal T, Brekken R, Isaksen JG. A fully-coupled fluid-structure interaction simulation of cerebral aneurysms. *Computational Mechanics* 2010; **46**(1):3–16. DOI: 10.1007/s00466-009-0421-4.
11. Perktold K, Rappitsch G. Computer simulation of local blood flow and vessel mechanics in a compliant carotid artery bifurcation model. *Journal of Biomechanics* 1995; **28**(7):845–856. DOI: 10.1016/0021-9290(95)95273-8.
12. Peskin CS. The immersed boundary method. *Acta Numerica* 2002; **11**:479–517. DOI: 10.1017/S0962492902000077.
13. Gerbeau JF, Vidrascu M, Frey P. Fluid-structure interaction in blood flows on geometries based on medical imaging. *Computers and Structures* 2005; **83**(2-3):155–165. DOI: 10.1016/j.compstruc.2004.03.083.
14. Figueroa CA, Vignon-Clementel IE, Jansen KE, Hughes TJR, Taylor CA. A coupled momentum method for modeling blood flow in three-dimensional deformable arteries. *Computer Methods in Applied Mechanics and Engineering* 2006; **195**(41-43):5685–5706. DOI: 10.1016/j.cma.2005.11.011.
15. Bazilevs Y, Calo VM, Zhang Y, Hughes TJR. Isogeometric fluid–structure interaction analysis with applications to arterial blood flow. *Computational Mechanics* 2006; **38**:310–322. DOI: 10.1007/s00466-006-0084-3.
16. Xiong G, Figueroa CA, Xiao N, Taylor CA. Simulation of blood flow in deformable vessels using subject-specific geometry and spatially varying wall properties. *International Journal for Numerical Methods in Biomedical Engineering* 2011; **27**(7):1000–1016. DOI: 10.1002/cnm.1404.
17. Moireau P, Xiao N, Astorino M, Figueroa CA, Chapelle D, Taylor CA, Gerbeau JF. External tissue support and fluid–structure simulation in blood flows. *Biomechanics and Modeling in Mechanobiology* 2012; **11**:1–18. DOI: 10.1007/s10237-011-0289-z.
18. Long CC, Hsu M-C, Bazilevs Y, Feinstein JA, Marsden A. Fluid–structure interaction simulations of the fontan procedure using variable wall properties. *International Journal for Numerical Methods in Biomedical Engineering* 2012; **28**(5):513–527. DOI: 10.1002/cnm.1485.
19. Hunt JCR, Wray AA, Moin P. Eddies, streams, and convergence zones in turbulent flows. *Center for Turbulence Research, Proceedings of the Summer Program 1998*, Stanford, CA, USA, 1988; 193–208.
20. Chong MS, Perry AE, Cantwell BJ. A general classification of three-dimensional flow fields. *Physics of Fluids* 1990; **2**(5):765–777. DOI: 10.1063/1.857730.
21. Jeong J, Hussain F. On the identification of a vortex. *Journal of Fluid Mechanics* 1995; **285**:69–94. DOI: 10.1017/S0022112095000462.
22. Alastruey J, Siggers JH, Peiffer V, Doorly DJ, Sherwin SJ. Reducing the data: analysis of the role of vascular geometry on blood flow patterns in curved vessels. *Physics of Fluids* 2012; **24**(3):031902-1–031902-24. DOI: 10.1063/1.3694526.
23. Cucitore R, Quadrio M, Baron A. On the effectiveness and limitations of local criteria for the identification of a vortex. *European Journal of Mechanics - B/Fluids* 1999; **18**(2):261–282. DOI: 10.1016/S0997-7546(99)80026-0.
24. Provenzale A. Transport by coherent barotropic vortices. *Annual Review of Fluid Mechanics* 1999; **31**:55–93. DOI: 10.1146/annurev.fluid.31.1.55.
25. Shadden SC, Taylor CA. Characterization of coherent structures in the cardiovascular system. *Annals of Biomedical Engineering* 2008; **36**(7):1152–1162. DOI: 10.1007/s10439-008-9502-3.
26. Morbiducci U, Gallo D, Ponzini R, Massai D, Antiga L, Montevecchi F, Redaelli A. Quantitative analysis of bulk flow in image-based hemodynamic models of the carotid bifurcation: the influence of outflow conditions as test case. *Annals of Biomedical Engineering* 2010; **38**:3688–3705. DOI: 10.1007/s10439-010-0102-7.
27. Liu X, Fan Y, Deng X, Zhan F. Effect of non-Newtonian and pulsatile blood flow on mass transport in the human aorta. *Journal of Biomechanics* 2011; **44**(6):1123–1131. DOI: 10.1016/j.jbiomech.2011.01.024.
28. Morbiducci U, Ponzini R, Rizzo G, Cadioli M, Esposito A, Montevecchi FM, Redaelli A. Mechanistic insight into the physiological relevance of helical blood flow in the human aorta: an in vivo study. *Biomechanics and Modeling in Mechanobiology* 2011; **10**(3):339–355. DOI: 10.1007/s10237-010-0238-2.
29. Masters JC, Ketner M, Bleiweis MS, Mill M, Yoganathan A, Lucas CL. The effect of incorporating vessel compliance in a computational model of blood flow in a total cavopulmonary connection (TCPC) with caval centerline offset. *Journal of Biomechanical Engineering* 2004; **126**(6):709–713. DOI: 10.1115/1.1824126.
30. Orlando W, Shandas R, DeGroff C. Efficiency differences in computational simulations of the total cavo-pulmonary circulation with and without compliant vessel walls. *Computer Methods and Programs in Biomedicine* 2006; **81**(3):220–227. DOI: 10.1016/j.cmpb.2005.11.010.

31. Maxey MR, Riley JJ. Equation of motion for a small rigid sphere in a nonuniform flow. *Physics of Fluids* 1983; **26**(4):883–889. DOI: 10.1063/1.864230.
32. Kenwright DN, Lane DA. Interactive time-dependent particle tracing using tetrahedral decomposition. *IEEE Transactions and Computer Graphics* 1996; **2**(2):120–129. DOI: 10.1109/2945.506224.
33. Shadden SC, Astorino M, Gerbeau JF. Computational analysis of an aortic valve jet with Lagrangian coherent structures. *Chaos* 2010; **20**(1):017512-1–017512-10. DOI: 10.1063/1.3272780.
34. Fontan F, Baudet E. Surgical repair of tricuspid atresia. *Thorax* 1971; **26**:240–248. DOI: 10.1136/thx.26.3.240.
35. de Leval MR, Kilner P, Gewillig M, Bull C. Total cavopulmonary connection: a logical alternative to atriopulmonary connection for complex Fontan operations. experimental studies and early clinical experience. *Journal of Thoracic and Cardiovascular Surgery* 1988; **96**(5):682–695.
36. de Leval MR, Dubini G, Migliavacca F, Jalali H, camporini G, Redington A, Pietrabissa R. Use of computational fluid dynamics in the design of surgical procedures: application to the study of competitive flows in cavo-pulmonary connections. *Journal of Thoracic and Cardiovascular Surgery* 1996; **111**(3):502–513.
37. Bove EL, de Leval MR, Migliavacca F, Balossino R, Dubini G. Toward optimal hemodynamics: computer modeling of the Fontan circuit. *Pediatric Cardiology* 2007; **28**(6):477–481. DOI: 10.1007/s00246-007-9009-y.
38. Dasi L, Pekkan K, Katajima H, Yoganathan A. Functional analysis of Fontan energy dissipation. *Journal of Biomechanics* 2008; **41**(10):2246–2252. DOI: 10.1016/j.jbiomech.2008.04.011.
39. Marsden AL, Bernstein AJ, Reddy VM, Shadden SC, Spilker RL, Chan FP, Taylor CA, Feinstein JA. Evaluation of a novel Y-shaped extracardiac Fontan baffle using computational fluid dynamics. *Journal Of Thoracic and Cardiovascular Surgery* 2009; **137**(2):394–U187. DOI: 10.1016/j.jtcvs.2008.06.043.
40. Marsden AL, Reddy VM, Shadden SC, Chan FP, Taylor CA, Feinstein JA. A new multiparameter approach to computational simulation for Fontan assessment and redesign. *Congenital Heart Disease* 2010; **5**(2):104–117. DOI: 10.1111/j.1747-0803.2010.00383.x.
41. Baretta A, Corsini C, Yang W, Vignon-Clementel I, Marsden A, Feinstein J, Hsia TY, Dubini G, Migliavacca F, Pennati G. Virtual surgeries in patients with congenital heart disease: a multiscale modelling test case. *Philosophical Transactions of the Royal Society A* 2011; **369**(1954):4316–4330. DOI: 10.1098/rsta.2011.0130.
42. Bazilevs Y, Hsu MC, Benson DJ, Sankaran S, Marsden AL. Computational fluid-structure interaction: methods and application to a total cavopulmonary connection. *Computational Mechanics* 2009; **45**(1):77–89. DOI: 10.1007/s00466-009-0419-y.
43. Schmidt J, Delp S, Sherman M, Taylor C, Pande V, Altman R. The Simbios National Center: systems biology in motion. *Proceedings of the IEEE* 2008; **96**(8):1266–1280. DOI: 10.1109/JPROC.2008.925454.
44. Hsia TY, Khambadkone S, Redington AN, Migliavacca F, Deanfield JE, de Leval MR. Effects of respiration and gravity on infradiaphragmatic venous flow in normal and Fontan patients. *Circulation* 2000; **102**(19 Suppl 3): 148–153. DOI: 10.1161/01.CIR.102.suppl_3.III-148.
45. Marsden AL, Vignon-Clementel IE, Chan FP, Feinstein JA, Taylor CA. Effects of exercise and respiration on hemodynamic efficiency in cfd simulations of the total cavopulmonary connection. *Annals of Biomedical Engineering* 2007; **35**:250–263. DOI: 10.1007/s10439-006-9224-3.
46. Spilker RL, Feinstein JA, Parker DW, Reddy VM, Taylor CA. Morphometry-based impedance boundary conditions for patient-specific modeling of blood flow in pulmonary arteries. *Annals of Biomedical Engineering* 2007; **35**:546–559. DOI: 10.1007/s10439-006-9240-3.
47. Greenfield JCJ, Griggs DMJ. Relation between pressure and diameter in main pulmonary artery of man. *Journal of Applied Physiology* 1963; **18**(3):557–559.
48. Bazilevs Y, Calo VM, Cottrell J, Hughes TJR, Reali A, Scovazzi G. Variational multiscale residual-based turbulence modeling for large eddy simulation of incompressible flows. *Computer Methods in Applied Mechanics and Engineering* 2007; **197**:173–201. DOI: 10.1016/j.cma.2007.07.016.
49. Justino H, Benson LN, Freedom RM. Development of unilateral pulmonary arteriovenous malformations due to unequal distribution of hepatic venous flow. *Circulation* 2001; **103**:e39–e40. DOI: 10.1161/01.CIR.103.8.e39.
50. Pike NA, Vricella LA, Feinstein JA, Black MD, Reitz BA. Regression of severe pulmonary arteriovenous malformations after Fontan revision and hepatic factor rerouting. *The Annals of Thoracic Surgery* 2004; **78**(2):697–699. DOI: 10.1016/j.athoracsur.2004.02.003.
51. Shadden SC. *Lagrangian Coherent Structures*, chap. 3. Wiley-VCH Verlag GmbH & Co. KGaA: Weinheim, Germany, 2011; 59–89. DOI: 10.1002/9783527639748.ch3.
52. Xu Z, Chen N, Shadden SC, Marsden JE, Kamocka MM, Rosen ED, Alber M. Study of blood flow impact on growth of thrombi using a multiscale model. *Soft Matter* 2009; **5**:769–779. DOI: 10.1039/B812429A.
53. Vetel J, Garon A, Pelletier D. Lagrangian coherent structures in the human carotid artery bifurcation. *Experiments in Fluids* 2009; **46**:1067–1079. DOI: 10.1007/s00348-009-0615-8.
54. Astorino M, Hamers J, Shadden SC, Gerbeau JF. A robust and efficient valve model based on resistive immersed surfaces. *International Journal for Numerical Methods in Biomedical Engineering* 2012; **28**(9):937–959. DOI: 10.1002/cnm.2474.
55. Shadden SC, Lekien F, Marsden JE. Definition and properties of Lagrangian coherent structures from finite-time Lyapunov exponents in two-dimensional aperiodic flows. *Physica D: Nonlinear Phenomena* 2005; **212**(3–4): 271–304. DOI: 10.1016/j.physd.2005.10.007.
56. Lekien F, Shadden SC, Marsden JE. Lagrangian coherent structures in n -dimensional systems. *Journal of Mathematical Physics* 2007; **48**(6):065404-1–065404-19. DOI: 10.1063/1.2740025.

57. Shadden SC, Dabiri JO, Marsden JE. Lagrangian analysis of fluid transport in empirical vortex ring flows. *Physics of Fluids* 2006; **18**(4):047105-1–047105-11. DOI: 10.1063/1.2189885.
58. Shadden S, Katija K, Rosenfeld M, Marsden J, Dabiri J. Transport and stirring induced by vortex formation. *Journal of Fluid Mechanics* 2007; **593**:315–332. DOI: 10.1017/S0022112007008865.
59. Eldredge JD, Chong K. Fluid transport and coherent structures of translating and flapping wings. *Chaos* 2010; **20**(1):017509-1–017509-14. DOI: 10.1063/1.3273036.
60. Mathur M, Haller G, Peacock T, Ruppert-Felsot JE, Swinney HL. Uncovering the Lagrangian skeleton of turbulence. *Physical Review Letters* 2007; **98**(14):144502-1–144502-4. DOI: 10.1103/PhysRevLett.98.144502.
61. Suh GY, Les A, Tenforde A, Shadden S, Spilker R, Yeung J, Cheng C, Herfkens R, Dalman R, Taylor C. Quantification of particle residence time in abdominal aortic aneurysms using magnetic resonance imaging and computational fluid dynamics. *Annals of Biomedical Engineering* 2011; **39**:864–883. DOI: 10.1007/s10439-010-0202-4.
62. Suh GY, Les A, Tenforde A, Shadden S, Spilker R, Yeung J, Cheng C, Herfkens R, Dalman R, Taylor C. Hemodynamic changes in abdominal aortic aneurysms with increasing exercise intensity using MR exercise imaging and image-based computational fluid dynamics. *Annals of Biomedical Engineering* 2011; **39**:2186–2202. DOI: 10.1007/s10439-011-0313-6.
63. Lonyai A, Dubin AM, Feinstein JA, Taylor CA, Shadden SC. New insights into pacemaker lead-induced venous occlusion: simulation-based investigation of alterations in venous biomechanics. *Cardiovascular Engineering* 2010; **10**(2):84–90. DOI: 10.1007/s10558-010-9096-x.
64. Kunov MJ, Steinman DA, Ethier CR. Particle volumetric residence time calculations in arterial geometries. *Journal of Biomechanical Engineering* 1996; **118**(2):158–164. DOI: 10.1115/1.2795954.
65. Taylor C, Steinman D. Image-based modeling of blood flow and vessel wall dynamics: applications, methods and future directions. *Annals of Biomedical Engineering* 2010; **38**:1188–1203. DOI: 10.1007/s10439-010-9901-0.
66. Conti C, Rossinelli D, Koumoutsakos P. GPU and APU computations of finite time Lyapunov exponent fields. *Journal of Computational Physics* 2012; **231**(5):2229–2244. DOI: 10.1016/j.jcp.2011.10.032.